

# Visualization of Underwater Shock Waves

Kazuyoshi Takayama

**Abstract** Results of optical flow visualizations of underwater shock waves performed in the Shock Wave Research Center of the Institute of Fluid Science in Tohoku University are presented. Underwater shock waves generated in ultrasound oscillations, underwater shock waves in two-phase shock tube flows, spherical shock waves in small scale underwater explosions, their interaction with gas bubbles and interfaces, and their reflection and focusing are visualized by single and double exposure holographic interferometry. Time resolved high-speed imaging revealed the luminous emission from a contracting gas bubble during shock/bubble interactions. It is concluded that double exposure holographic interferometry can be very effective for quantitative observation of underwater shock waves, and that high-speed time resolved imaging can be useful for the underwater shock wave research.

## 1 Introduction

Underwater shock waves are generated not only in nature but also in the artificial world from micro-scale events such as the collapse of microscopic bubbles to the gigantic explosion of magma-water vapor during volcanic eruptions. Hence, the underwater shock wave research is one of the highlights of shock dynamics. However, unlike shock wave in gases, the optical visualization of shock waves in liquids is not as simple as those in gases, because of the higher degree of inhomogeneity of liquids. Likewise, the generation of strong shock waves in liquids is not necessarily as straightforward as that of gases, because the acoustic impedance of liquids is significantly larger than that of gases.

In this chapter, the author will demonstrate some of underwater shock wave phenomena he collected throughout forty years of his shock wave research: shock

---

K. Takayama (✉)  
Institute of Fluid Science, Tohoku University, 2-1-1 Katahira, 980-77 Aoba Sendai, Japan  
e-mail: k.takayama@mac.com

waves generated during ultrasound oscillatory tests; underwater shock waves produced in shock tubes; underwater micro-explosions; and shock/bubble interactions associated with underwater explosions.

## 2 Ultrasound Oscillation

We dipped a 16 mm diameter 304 stainless steel specimen into water at 3 mm depth. The test water was ion exchanged and contained in a test chamber of 200 mm in diameter and 150 mm in width. The specimen was driven with a 500 W ultrasonic vibrator. The displacement  $x$  of the specimen surface is described as  $x = \tilde{A}\sin\omega t$ , where  $\tilde{A}$  is the half amplitude of 17.5  $\mu\text{m}$ , and  $\omega$  is frequency of 17.7 kHz.

We visualized oscillatory flows by using a single exposure image holography with a light source of double pulse holographic ruby laser (Apollo Laser Inc. 22HD). The light source was coherent and had a pulse width of 25 ns. Although the holographic images were still just observation, we synchronized the images correctly with the phase angle of the vibrator at every  $\pi/4$  rad and collected sequential images of flows. Although we had taken high-speed photography, still images we collected had a much finer resolution than that of high-speed photography.

We took streak recordings at the rate of 1.5  $\mu\text{s}/\text{mm}$  and frame recordings at the rate of 200,000 fps (frames/s) by using Ima-Con John Hadland 790. The magnification of the images was 0.594. We used a 500 mW Argon-ion laser as a light source and synchronized its operation with a mechanical shutter of 1 ms opening duration. In the streak recordings, we put a slit of 0.75 mm in width exactly on the surface of the specimen. The slit width observable in the streak images was 0.44 mm.

Figure 1 shows the streak image. The ordinate designates the distance along the surface of the specimen in mm and the abscissa designates time in  $\mu\text{s}$ . When the specimen starts to pull water at  $\omega t = \pi/4$ , the deceleration starts and the deceleration force— $A\omega^2$  is a maximum, equivalent to  $-6G$ , which locally generates the tensile stress of water. Hence, cavitation bubble inception would take place depending on the distribution of cavitation nuclei in water.

The grey shadow in Fig. 1 indicates variation of the density of the bubble cloud. The increasing grey shadow would indicate at first the increase of number density

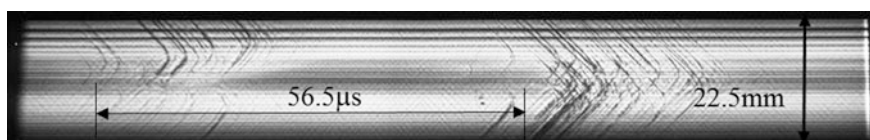


**Fig. 1** Streak recording of oscillatory flows at 103 kPa, 293 K. The ordinate: the distance along the surface of the specimen in mm, the abscissa: time in  $\mu\text{s}$

and at the same time growth of their size and hence the resulting grey shadow would be a maximum at around  $\omega t = \pi/2$ . Then the grey zone indicates the contraction of the bubbles, which were exposed to the compression waves at  $\omega t > \pi/2$ .

Exposed to pressure fluctuations, bubbles started to contract and eventually became a minimum volume and the pressures became highest. In the case of axially symmetric bubbles, the high pressures are induced by adiabatic compression. Then the high pressures drive so-called rebound shock waves. In the case of asymmetric bubble contractions, the bubble motion is based on the propagation and focusing of shock waves inside the bubbles. As the shock compression creates high pressure much more efficiently than the adiabatic compression, the shock wave motion would contribute to the high pressure generation.

Anyway, the higher pressures in the bubble were released into water as a train of compression waves, which instantaneously coalesced into an underwater shock wave. This may be reproducible by a fine numerical simulation.

Trajectories of shock waves view through 0.75 mm thick slit are shown as shallow V shaped lines randomly distributed in the region where the grey shadow faintly diminishing. The streak image was viewed through a width of 22.5 mm. One cycle of oscillation is 56.5  $\mu\text{s}$  as described in Fig. 1. Images in the neighborhood of the diameter looked sharpest and those on the frontal and rear edges are blurred.

The creation and diminishment of bubbles are not necessarily exactly regulated by the specimen's movements. Looking at the series of streak recordings at identical initial conditions, it is found that the evolution of each bubble has its own history. The bubble collapse may belong rather to a stochastic process and is not precisely regulated by the specimen's movement. Therefore, the shock wave formations would occur slightly randomly as seen in Fig. 1.

Sanada et al. [1] measured the evolution of a sharply observable trajectory in the x-t plane and estimated that the shock Mach number  $M_s$  varied from its initial value of about 1.5 to a sound wave of  $M_s = 1.0$ . Assuming a planar underwater shock, its overpressure at  $M_s = 1.5$  would be well over 500 MPa. Such a high pressure working on a spot would readily erode the metal surface.

In Fig. 2a–d, images of the generation and diminishment of bubbles and the formation and disappearance of shock waves at 285 K and 0.2 MPa are presented at individual phase angles. Figure 2a shows the bubble creation at a stage of  $\omega t = \pi/2$ , at which bubbles are created and impulsively ejected from the edge of the specimen. Columns of bubble cloud are formed at the center of the specimen, when the specimen's receding speed is a maximum. That the eight-digit figure, for example, attached to Fig. 2a, #82112502, indicates that we visualized this image in 1982, November, 25th, the test No. 2. Note that the surface deformation in reality does not show a simple mode but would show a complex surface pattern. Hence the resulting bubble column distributions are not always uniform. Then we see no bubbles being generated on the edge.

In Fig. 2a, we find a semi-circle marked by B. Measuring the radius of the semi-circle, this is a remnant of a shock wave generation which was created by a bubble collapse at 2.7  $\mu\text{s}$  prior to this observation. A circle marked by A, whose

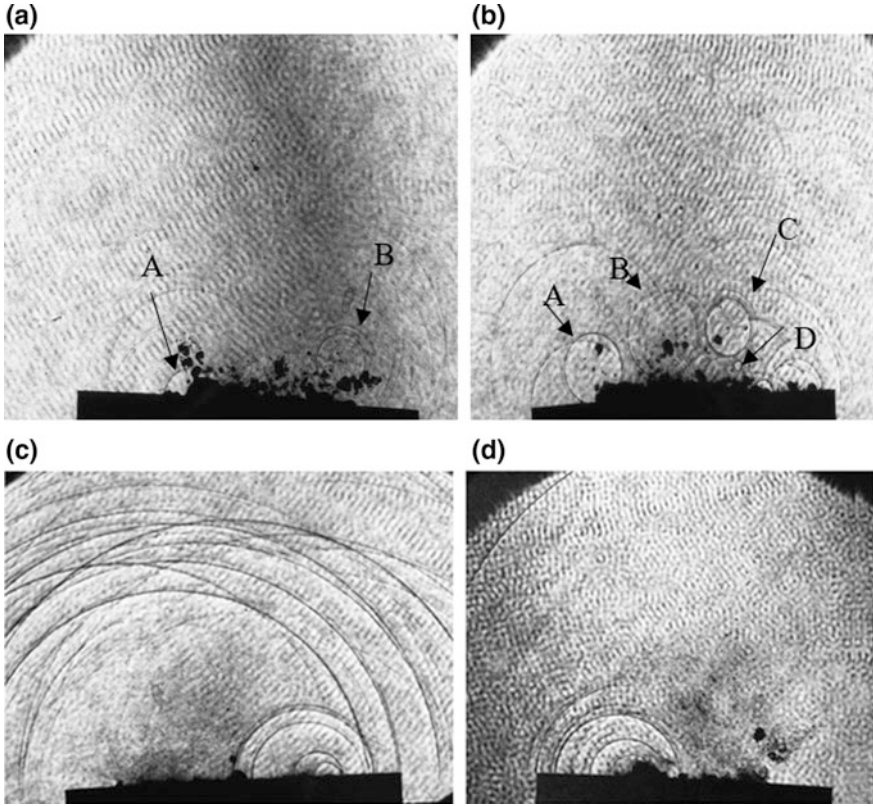


**Fig. 2** Single exposure holographic images of a ultrasonic oscillation at 285 K, 0.2 MPa: **a** #82112502, at the phase angle of  $\pi/2$ ; **b** #82112503, at  $3\pi/4$ ; **c** #82112505, at  $5\pi/4$ ; **d** #82112506, at  $3\pi/2$

center is located a few mm above the specimen, is a weak shock wave created  $0.8 \mu\text{s}$  prior to this observation.

The surface of the specimen moves repeatedly at a speed with amplitude of  $\tilde{A}\omega$  and eventually induced convective flows in the entire flow field. Therefore, bubbles so far accumulated and surviving throughout the oscillatory motion are drifted along the center line. The grey shadow in the central region above the oscillator indicates the integrated images of bubble clouds.

Figure 2b shows the stage at  $\omega t = 3\pi/4$ . The bubble inception and resulting shock formation in oscillatory tests is, in principle, synchronized with the phase angle of the oscillator, but is subjected to the stochastic procedure. Hence, in Fig. 1, we identify, regardless of faintly observable shock wave trajectory or distinctly visible shock trajectories, resulting shock waves all the time. Figure 2c shows that the bubbles collapsed and the appearance of shock wave at  $5\pi/4$ , and Fig. 2d at  $3\pi/2$ .

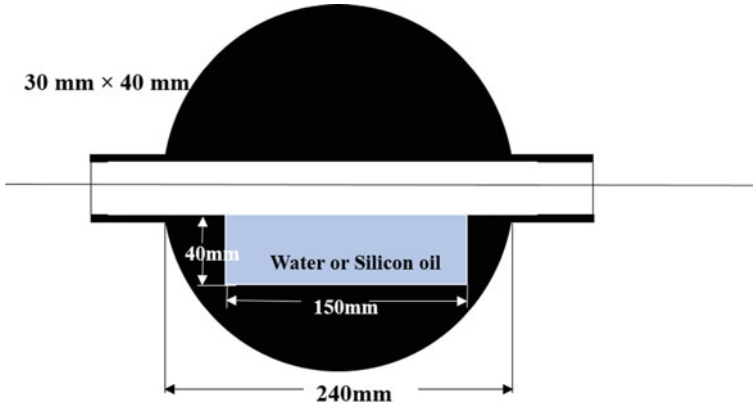


Fig. 3 A test section filling liquids in its bottom [2]

### 3 Shock Tube Flows

Firstly, we will observe underwater weak shock waves by means of a conventional shock tube. Figure 3 shows a test section made of stainless steel, the bottom filled with water or silicon oil TSF-10 of sound speed of 968 m/s at 293 K.

The test section was connected to a 30 mm × 40 mm shock tube. We filled silicon oil TSF-10 in the bottom of the test section. The surface of the liquid layer was very flat but was receded a few mm from the bottom of the shock tube due to the surface tension of the liquid.

In Fig. 4, we visualized the shock tube flows by using a double exposure holographic interferometry. The fringes correspond to equal density contours [3]. It should be noticed that double exposure holographic interferometry is very useful to quantitative measurements of the two-dimensional shock wave phenomena, in particular, in liquids. Individual fringes of infinite fringe interferograms correspond to changes in phase angles which occur only during double exposures. Defects of test sections are insensitive to the measured image data. Especially background noises induced by natural convections or low frequency vibrations of experimental setup can be readily eliminated, if the interval of double exposures is set very short.

In Fig. 4a, b, we can see shock waves in air propagating over TSF-10 layers: (a) shock Mach number  $M_s = 2.97$  and its propagation speed  $U_s$  of 1127 m/s, supersonic in terms of the sound speed in silicon oil,  $a_{silicon} = 960$  m/s; and (b)  $M_s = 2.70$  and propagation speed of 896 m/s, subsonic in terms of  $a_{silicon} = 960$  m/s.

Figure 4a shows that the shock wave being supersonic in terms of  $a_{silicon}$ , an oblique shock is observable in silicon oil, whose inclination angle  $\phi$  is  $\sin\phi = a_{liquid}/U_s$ . Behind the oblique shock, we can see three fringes which imply gradual density decrease or pressure decrease toward the lower wall. Then the oblique shock is attenuated to be sonic wave in the neighborhood of the bottom wall.

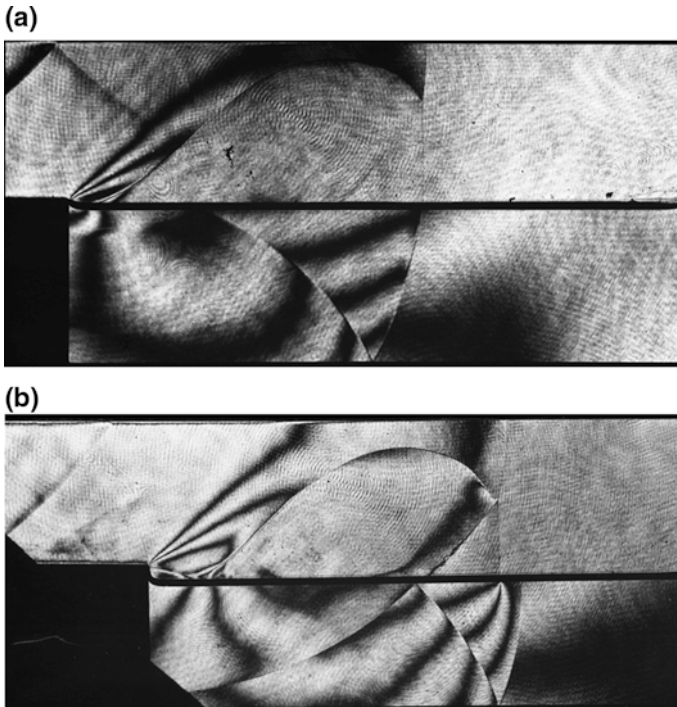


**Fig. 4** Shock/silicon oil layer interaction: **a** #81052703,  $M_s = 2.969$  at 123 hPa and 294.4 K in air; and **b** # 81051901,  $M_s = 2.701$  at 150 hPa and 288.2 K in air

Figure 4b shows a subsonic case. A sound wave in silicon oil propagates much faster than the shock wave in air. The front of a precursory sound wave is presented to be a faint change in fringe. From the front of the precursory sound wave, the pressure gradually increases to the foot of the shock on the surface of the silicon oil, which is apparently a singular point as the fringes concentrate.

In gases, patterns of reflected shock waves over solid walls uniquely transit between regular reflection and Mach reflection, depending on the shock Mach number, reflection angles and the specific heat ratio of gases [4]. We were interested in the effect of wall conditions on the reflected shock transition. Hence, to test the transition over a liquid wedge which is perfectly flat and admit slip conditions on the wall surface, we inclined the entire 30 mm  $\times$  40 mm shock tube and the water filled test section. We eventually formed a water wedge [5] and visualized, by using double exposure holographic interferometry, shock wave reflection over water wedges. In Fig. 5a, b, we can see shock waves at  $M_s = 2.27$  reflected from a water wedge: (a) transitional Mach reflection (TMR) from a 46.2° wedge; and (b) regular reflection (RR) from a 40.0° wedge. The speed  $u$  of the foot of the shock wave along the water wedge,  $u = U_s \cos \theta \leq a_{water}$ , is subsonic but closer to  $a_{water}$ , then we can see a sonic front which, although very faint, is clearly identified as a

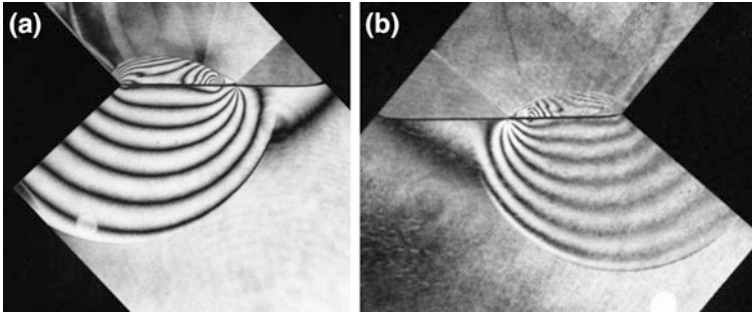


**Fig. 5** Shock wave reflection over water wedges: **a** #85061701,  $M_s = 2.293$  at 710 hPa and 294.7 K in air,  $46.2^\circ$ , TMR; and **b** #85061502,  $M_s = 2.258$  at 710 hPa and 294.3 K in air,  $49.0^\circ$ , RR

precursory discontinuous front appearing in a finite distance. This trend is more clearly observable for the wedge angle of  $49.0^\circ$  as seen in Fig. 5b.

## 4 Underwater Explosions

The conservation equations of gas-dynamics in a continuum can be summarized by the following equation:  $\delta p = a \rho \delta u$ , where  $\delta p$ ,  $a$ ,  $\rho$  and  $\delta u$  are pressure perturbation, sound speed of the medium under discussion, density, and velocity perturbation.  $a\rho$  is defined as acoustic impedance which indicates the degree of the compressibility of media. Therefore, for a given pressure perturbation, a medium having smaller acoustic impedance can induce a larger velocity perturbation than in a medium having larger acoustic impedance. As  $(a\rho)_{\text{water}}/(a\rho)_{\text{air}} = 3700$ , water is much less compressible than gases. Hence, it is not easy to safely generate an underwater explosion, especially, in laboratory scale experiments. In 1968, Glass and Heuckroth [6] ruptured thin wall glass spheres in water and succeeded to generate spherical underwater shock waves. He tried to visualize, by using the Schlieren method and recording with multi-frame camera, the transition of reflected underwater shock waves. As the shock waves which so far he produced were so weak, the pattern of reflected spherical shock waves was a regular reflection. Figure 6 shows sequential visualization of two underwater shock waves and their interaction.

Finishing a training of safe synthesizing lead azide, we eventually produced in house micro-pellets weighing from a few mg to 10 mg ( $\text{PbN}_6$ : density, 1.5 g/cc, detonation speed, 2.98 km/s). We had a permission from the government of handling micro-explosives in laboratory and ignited them in liquid by illuminating them with a Q-switch laser beam. Later, the Chugoku Kayaku Co. Ltd kindly provided us with 10 mg silver azide pellets, ( $\text{AgN}_3$ : density, 3.8 g/cc; detonation speed, 5.05 km/s; ignition energy,  $30 \mu\text{J}/\text{mm}^2$ ), for supporting our application of underwater shock wave focusing the disintegrate of urinary tract stones.

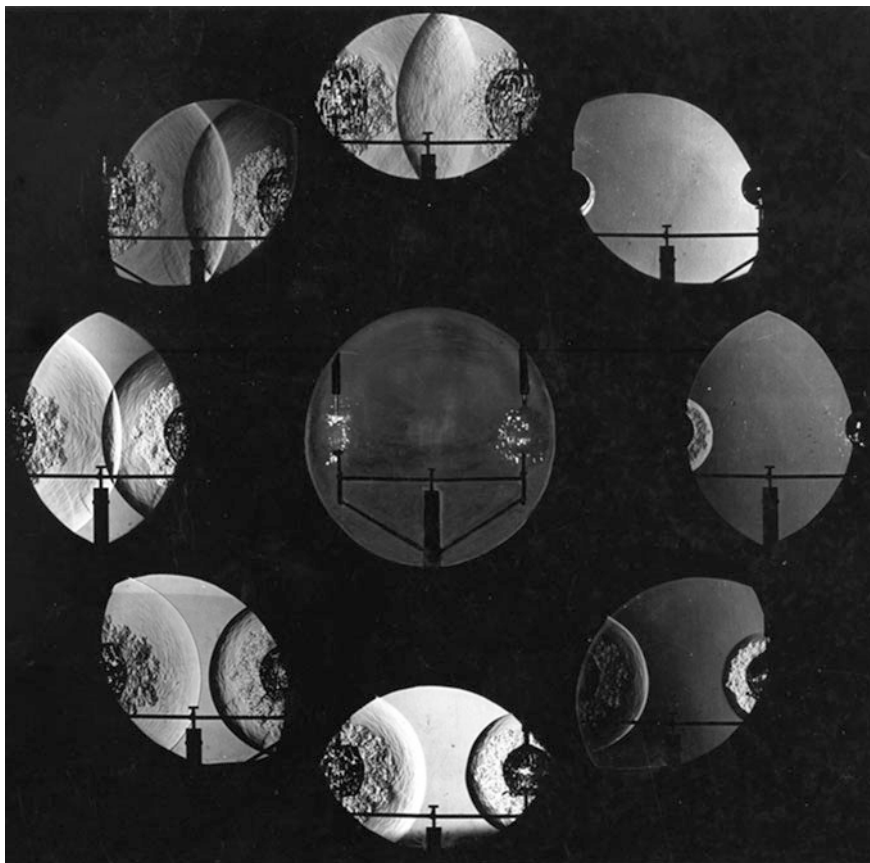


**Fig. 6** Interaction of two weak shock waves reproduced from [6], with the permission of AIP Publishing

At first, we glued explosive pellets on a cotton thread and suspended it in water. We visualized underwater shock waves by using double exposure holographic interferometry. Figure 7a shows an underwater shock wave driven by 4 mg of lead azide. A small dark spot in the middle and a thin vertical line show the pellet and the cotton thread, respectively. The grey circle in the middle shows the detonation product gas. The spherical shock wave is visualized to have circular shape.

Beautifully, axial symmetrical spherical fringes appear. These were formed as integral of the light beams crossing along the path from a shock front to its reverse front, now look like co-axial fringes. The fringes are packed very densely just behind the shock front but still have spatial resolution. Assuming axial symmetric flows, we counted, from the shock front to the boundary of the detonation product gas, the order and interval of fringes on a magnified interferogram as seen in Fig. 7a. From the data, we can determine the density profile and then the pressure



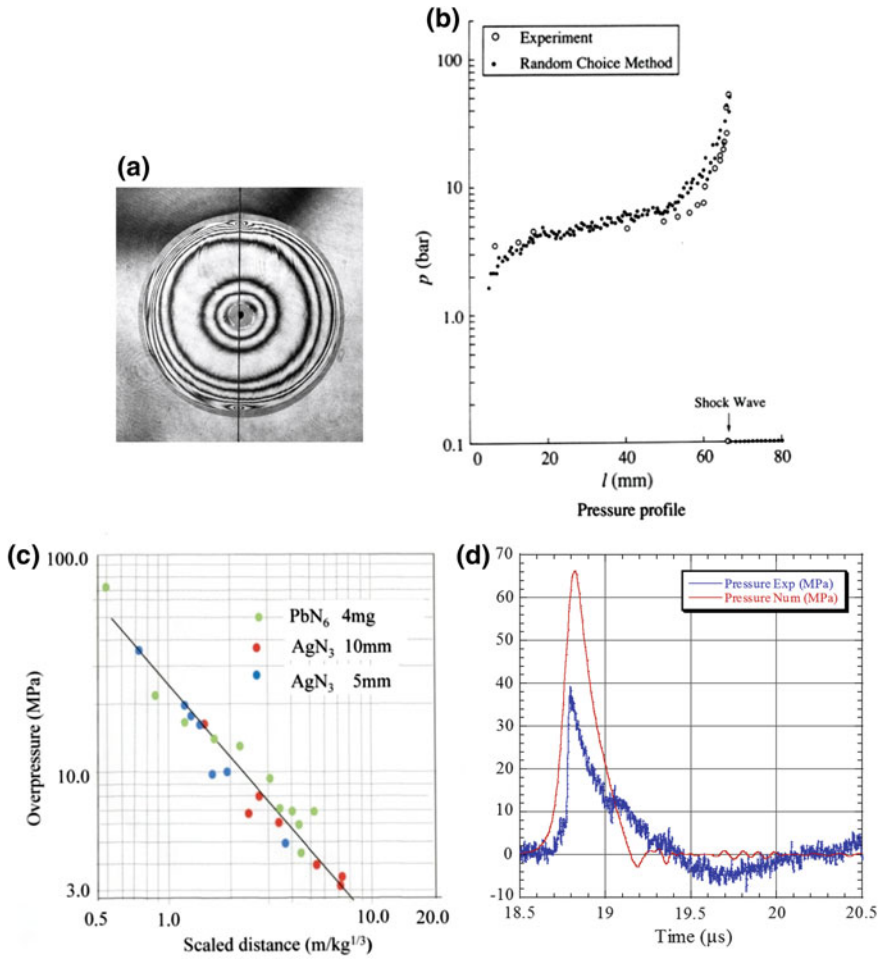


**Fig. 7** Underwater explosion: **a** Interferogram, 4 mg lead azide explosion; **b** Pressure profile; **c** Overpressure-scaled distance correlation of underwater micro-explosion; **d** Comparison between the measured pressure variation and numerical simulation [9]

profile by using the Tait equation [7]. Figure 7b shows the pressure profile estimated from Fig. 7a and the comparison with the random choice numerical simulation. It should be noted that we matched the density at the shock front with the simulated value, as this value cannot be estimated from the fringe counting.

Later, our experimental skill was so refined as to attach micro-pellets on the tip of 0.6 mm diameter optical fiber. Explosives weighing even 3  $\mu\text{g}$   $\text{AgN}_3$  were detonated by irradiating them with a Q-switched Nd:YAG laser beam of energy of 20 mJ and pulse width of 7 ns. The total energy of 3  $\mu\text{g}$   $\text{AgN}_3$  is about 5 mJ, and such a small grain of  $\text{AgN}_3$  still obeys the scaling law.

Figure 7c shows the relationship between overpressure (MPa) and scaled distance ( $\text{m}/\text{kg}^{1/3}$ ). Black circles designate overpressure in MPa of 4–10 mg lead azide pellet measured at the stand-off distance from 5 to 80 mm [8]. Red circles designate overpressure of silver azide from 3 to 300  $\mu\text{g}$  measured at the stand-off distance of 10 mm from the explosives, and blue circles designate overpressure of silver azide of 3 to 300  $\mu\text{g}$  measured at the stand-off distance of 5 mm from the explosives. Overpressures were measured by a fibre optics hydrophone (FOPH), in which the pressure was detected not by piezo effect but by optically detecting the change in the phase angle of the spot to measure between the reference and object laser beams.

Figure 7d shows the time variation of shock wave overpressures caused by a 30  $\mu\text{g}$   $\text{AgN}_3$  explosion. The pressure was measured by the FOPH, which had a time resolution of 10 ns and a diameter of 0.2 mm. The time variation of the overpressure profile is similar to that of 10 mg  $\text{AgN}_3$  explosion. A red thin line indicates a result of numerical simulation by using a finite difference scheme [9]. The modeling of underwater explosion of silver azide was not quantitatively tuned yet so that the trend of time variation of pressures agreed between the simulation and the experiment.

Figure 8a shows a sequential direct shadowgraph of a shock wave created by the detonation of 10 mg  $\text{AgN}_3$  attached at the edge of a 0.6 mm core diameter and

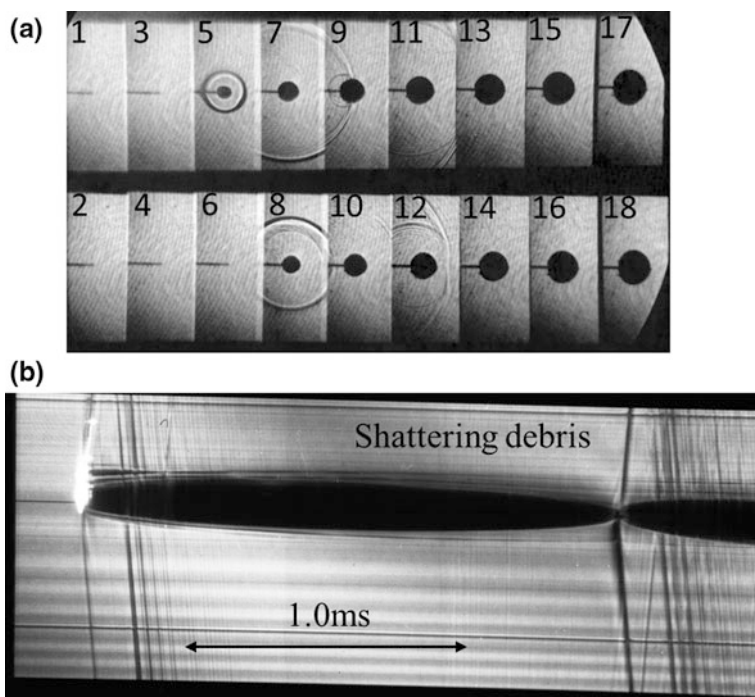


**Fig. 8** Formation of shock waves by micro-explosions of 10 mg  $\text{AgN}_3$ : **a** #90070702, framing photograph 100,000 fps; **b** #85121729 streak recording

1.5 mm sheath diameter optical fiber. The images were taken by Ima-Con 970 at the framing rate of 100,000 fps. Upon the laser irradiation,  $\text{AgN}_3$  was detonating and its detonation product gas formed a dark circle which expanded at supersonic speed and hence drove a spherical shock wave shown as a white circle. It immediately moved away from the view and about 20  $\mu\text{s}$  later, was reflected from the neighboring solid wall. The reflected shock interacted with the detonation product gas. The thin dark circular curve seen in the 10th and 11th frames showed reflected expansion wave from the bubble which was induced due to the acoustic impedance mismatching at the water/gas bubble interface. On the 11th frame, the part of the reflected shock wave, which was interacted with the reflected expansion wave, was significantly deviated from the circular. That is, the reflected shock was attenuated.

Such complex interfacial reflections and long term behaviors of the detonation product gas is demonstrated in a streak recording in Fig. 8b. The ordinate designates the length scale and the abscissa designates the elapsed time. A dark shadow shows the evolution of the detonation product, the gas bubble. A bright spot at the left hand side indicates the explosion, and a resulting shock wave is shown by a dark line.

A dark line appearing from the upper part at 20  $\mu\text{s}$  later was a reflected shock from a neighboring solid wall. When reaching a maximum diameter, the detonation product gas bubble started to contract. Minute fragments or debris of unburned chemical components shattered outward at nearly the detonation speed. The debris overtook the bubble surface when it started to contract. This is shown as grey clouds to be seen in Fig. 8b. When the debris shattering terminated, the bubble diameter was a minimum and started to explosively expand, driving trains of compression waves, which eventually coalesced into secondary shock waves.

## 5 Shock/Bubble Interaction

Wave interactions in high-speed gas flows can decrease pressures even down to vacuum, whereas wave interaction in liquids can also decrease pressures but down to their evaporation pressure. When exposing liquids to pressures lower than the evaporation pressure, a rapid phase change would be induced. This is a spontaneous bubble formation which we already saw in the ultrasonic oscillation. The bubble inception occurring in hydraulic machineries are named as cavitation. The fundamentals of cavitation research are called the bubble dynamics, which is one of the highlights of underwater shock wave research. Underwater shock wave research is very closely linked with bubble dynamics. Shima reviewed the bubble dynamic research [10]. Firstly, we decided to examine shock interaction with a single bubble. We released 1.7 mm diameter spherical air bubbles rising vertically at 0.17–0.22 m/s from the bottom of the water chamber. The bubbles were released from a thin syringe needle by keeping the release pressure difference smaller, so that we maintained spherical bubbles. For bubbles whose shapes significantly deviated from a spherical shape, the response of their motion to the shock wave would differ from that of spherical ones.

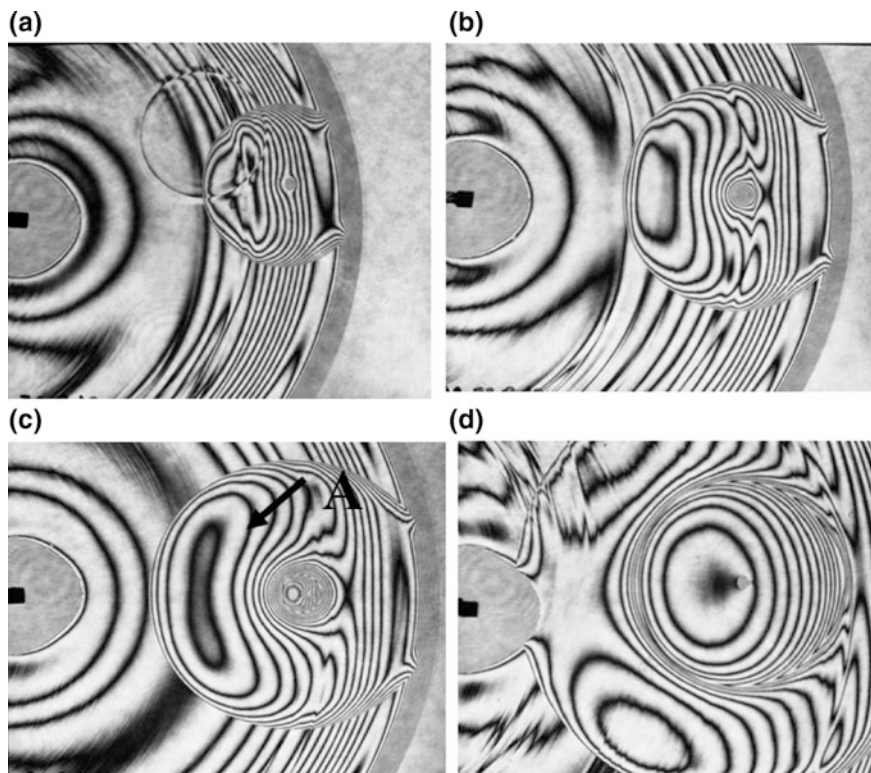


**Fig. 9** Shock/bubble interaction, shock waves were generated by the detonation of 10 mg  $\text{AgN}_3$ : **a** #86082507, delay time: 18.4  $\mu\text{s}$ ; **b** #86082506, delay time: 20.1  $\mu\text{s}$ ; **c** #86082505, delay time: 22.1  $\mu\text{s}$ ; and **d** #86082504, delay time: 23.1  $\mu\text{s}$

We generated underwater shock waves by detonating a 10 mg  $\text{AgN}_3$  pellet attached at the tip of optical fiber [7]. At the 20 mm stand-off distance, its overpressure would be about 50 MPa. We visualized the procedures of shock/bubble interactions by both single exposure holograms and double exposure holographic interferometry. The fringe distributions are axially symmetrical and hence, if we count correctly the fringe order and distributions, we can estimate experimentally the pressure profiles from interferograms [7].

Figure 9a–d show sequential double exposure holographic interferograms. Measuring the radius of the reflected expansion wave Fig. 9a was taken after the incident shock hit the air bubble. Figure 9a was taken at about 4  $\mu\text{s}$  after the incident shock hit the air bubble. When the shock wave of overpressure of 50 MPa passed the bubble, it immediately started to contract. Its reaction, the expansion wave was released into surrounding water, which propagated in water at its sonic speed. This is the reflected expansion wave. At the same time, a transmitting shock propagates inside the bubble. This situation will be discussed later.

In Fig. 9b, we can see that the expansion wave is driven by the contraction of the air bubble. Double exposure holographic interferometric images show the phase difference of light beams which recorded phase distributions of images before and after the event. A reference image before the event and an object image that recorded the event are superimposed in a hologram. In the present case, the images of the original bubble and the contracting bubble are superimposed and hence we do not see the contracting bubble shape. We can detect these bubble deformations but clearly identify the fringe concentration at the frontal stagnation point of the bubble.

Figure 9c was taken at  $6.7 \mu\text{s}$  after the incident shock impingement on the bubble; the time was calculated from the image. Note that the delay time described in the figure caption includes measurement deviation. Fringes are densely accumulated on that side, which indicates the local pressure increase. When the pressure was a maximum, a train of compression waves was released, which coalesced into a secondary shock wave. In reality, the center of the flat side was not planar but protruded toward the inside. Such a deformation was driven by the high pressure which accumulated at this side.

Eventually the formation created a water jet penetrating the bubble. Figure 9d shows interferogram at  $11.2 \mu\text{s}$  (estimated from the image) after the shock impingement on the bubble. We can see the water jet penetrating the bubble. It should be noticed that the grey shadow shows the combination of the original bubble and the jet and the real recovering bubble shape was much too small.

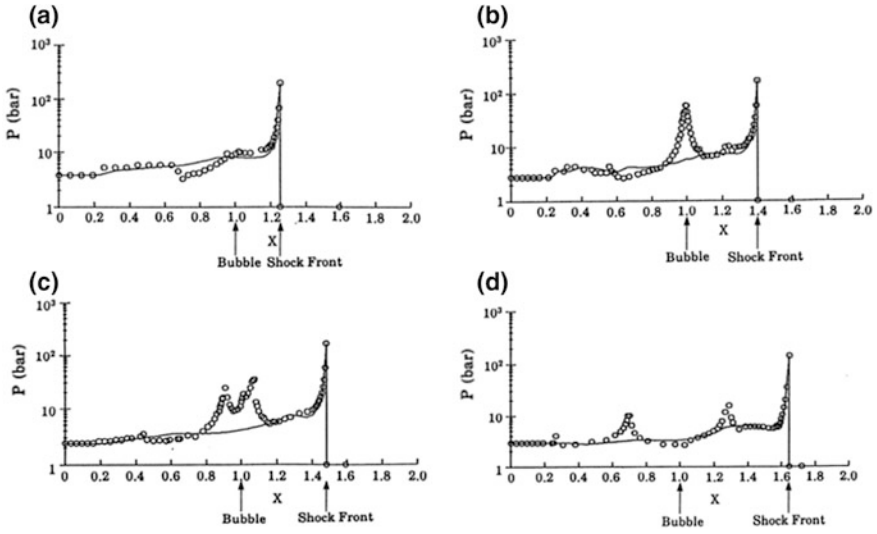
The jet speed varied depending on the bubble diameter and the loading pressure. It is known that if a shock wave of overpressure of a few hundred MPa is loaded on a 2.0 mm air bubble, the resulting jet speed can be about 100 m/s. Hence, the resulting stagnation pressure,  $p_{stagnation} = \rho u^2$ , will be about 150 MPa.

Counting the fringe intervals and the fringe orders of the interferograms shown in Fig. 9a–d, we can calculate, by assuming the axial symmetric field, the pressure profiles over the bubbles in Fig. 10a–d, respectively. We can see the pressure decrease across the reflected expansion wave and the gradual accumulation of high pressure on the side at which the shock impinged. Then the high pressure was released as trains of compression waves, whose coalescence then formed a secondary shock wave.

For bubbles of, for example,  $10 \mu\text{m}$  diameter, their impingement by shock waves would follow a different scenario as described in Fig. 10. The reflected expansion wave is immediately overtaken by the secondary shock wave. Hence, the shock/bubble interaction would create secondary shock waves.

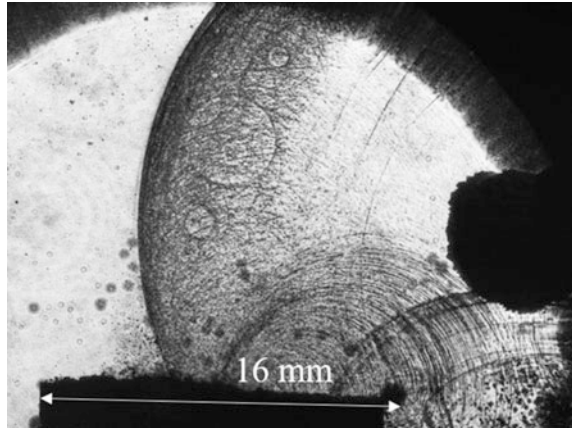
## 6 Shock/Bubble Cloud Interaction

Figure 11 shows the interaction of a spherical shock wave with, presumably, the densest bubble cloud observed. In Fig. 5, we already observed the bubble cloud densely migrating over the ultrasonic oscillator. At this instant, we load a strong shock wave onto the bubble cloud by detonating 10 mg  $\text{PbN}_6$  attached on the tip of



**Fig. 10** Pressure profiles of shock/bubble interaction displayed in Fig. 9: **a** Fig. 9a, 18.4  $\mu$ s; **b** Fig. 9b, 20.1  $\mu$ s; **c** Fig. 9c, 22.1  $\mu$ s; and **d** Fig. 9d, 23.1  $\mu$ s

**Fig. 11** Shock interaction with bubble clouds at 0.1 MPa and 301 K: #821129, delay time 73  $\mu$ s



the optical fiber at about 10 mm away from the edge of the oscillator. The overpressure was about 50 MPa at a stand-off distance of 20 mm.

Upon shock loading, all the bubbles instantaneously collapsed and converted into shock waves. Circles and semi-circles in Fig. 11 are the resulting shock waves. Although we did not recognize many bubbles migrating above the oscillator, now we saw so many rings distributed behind the shock wave. We can see that the bubbles on the oscillator surface collapsed by the shock wave loading.

A bubble curtain is one of the best methods of mitigating underwater shock waves. Their diameters and spatial distributions would be important parameters to

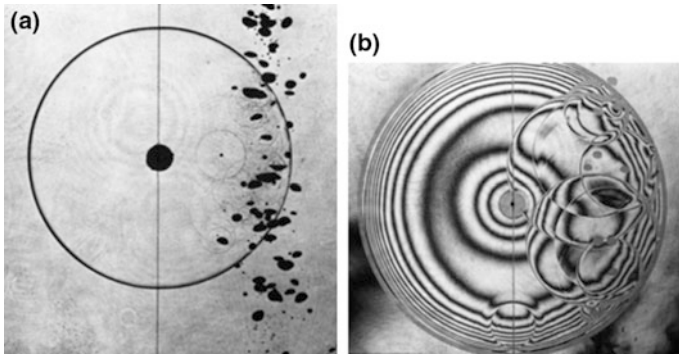


**Fig. 12** Shock bubble/cloud interaction  $\text{PbN}_6$  10 mg, stand-off distance of 20 mm: **a** #83013117, single exposure hologram; **b** #83013103, double exposure interferogram

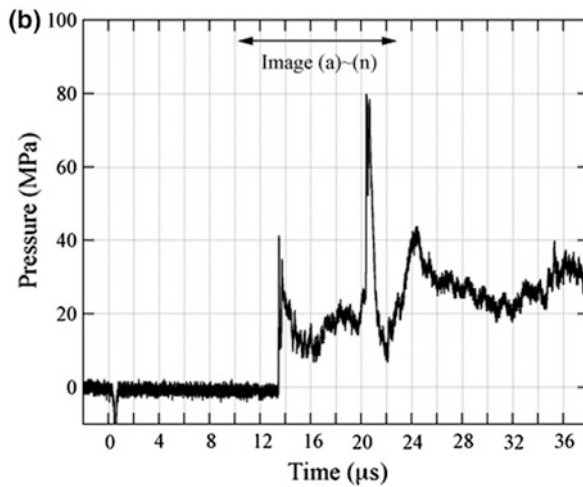
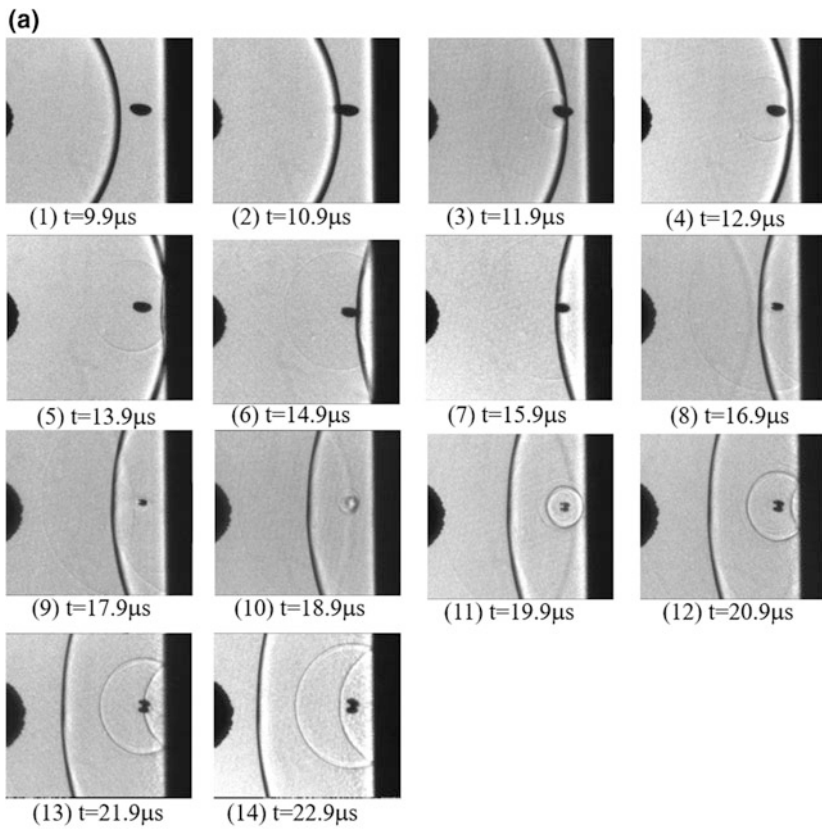
design the bubble curtains. In Fig. 12, we visualized, by using single exposure holography and double exposure holographic interferometry. Air bubbles were ejected from a 1.0 mm diameter nozzle placed at the bottom of a water chamber. Hence bubbles had not necessarily spherical shape but randomly oriented ellipsoidal shape. Shock waves were generated by explosion of 10 mg  $\text{PbN}_6$  and loaded at the stand-off distance of about 20 mm. The loading pressure was about 50 MPa.

Figure 12a shows a single exposure. The shock front was displayed as a broad dark ring. However, when it was caught up with the reflected expansion wave, the broad ring shape became thin. This implies that the shock front is locally attenuated. Such attenuations occurred over the bubble surface at which the shock passed the air bubbles.

Figure 12b shows a double exposure holographic interferogram. As seen in Fig. 9a–d, when the shock wave hit a large air bubble, it deforms and creates distinct reflected expansion wave. Along the part of the shock front at which the expansion wave interacted, the number of fringes drastically decreased, which implies that shock wave is attenuated.

## 7 Luminous Spot at Shock/Bubble Interaction

An ellipsoidal bubble of a major diameter of 2.5 mm and a minor diameter of 1.5 mm positioned at 5 mm from a solid wall started to collapse, when it was loaded at its minor diameter by a shock wave generated by explosion of a 10 mg  $\text{AgN}_3$  pellet which was attached at the tip of an optical fiber. At the 20 mm stand-off distance, the overpressure was about 50 MPa. Figure 13a shows a sequential direct shadowgraph of 1.0  $\mu\text{s}$  inter-frame time and exposure time of 10 ns by using Ima-Con 200. A 0.4 mm diameter optical fiber hydrophone was imbedded in the solid wall.



**Fig. 13** Emission of luminosity at shock/bubble interaction: **a** Sequential observation; **b** pressure measurement [11]



The shock wave propagated from the left-hand side. In the second and third frames, we can see the transmission of the shock wave over the bubble. The bubble started to contract from the third frame. We can see the reflected expansion wave, which was so faint to be hardly identified. In the sixth frame, the shock wave was reflected from the wall. In the seventh and eighth frames, the bubble interacted with the reflected shock wave. The bubble contraction continued. At the ninth frame, the bubble had a minimum volume and its shape looked slightly irregularly deformed. In the tenth frame, the rear part of the bubble was shining. The bubble started to expand.

In the eleventh frame, the secondary shock wave, rather strong, was generated. So far estimated from the distance it travelled with the velocity of about  $M_s = 1.67$ . In the twelfth frame, the bubble expanded with an elapse of time and  $M_s = 1.49$ . Sanada et al. [1] estimated, from a trajectory of shock formation in streak images in ultrasonic oscillatory tests, the attenuation of a shock wave. When a bubble collapsed, the initial shock Mach number was about 1.5, which immediately attenuated to sonic speed. The Mach number of the secondary shock wave took nearly the same value.

In these frames, the bubble deformed so as for its frontal side to penetrate toward the inside of the bubble. The jet speed so far measured was in the order of magnitude of 100 m/s, which would produce the stagnation pressure of about 150 MPa, as already observed in the case of the shock/single bubble interaction in Sect. 5.

At the side of the bubble where the shock impinged, the pressure was so enhanced that it formed a jet. At the same time, the high pressure outside the bubble, say 50 MPa, is transmitted into the gas inside the bubble. When a high pressure of 50 MPa is transmitted into air or water vapor inside the bubble, very strong shock waves must be induced. When such a strong shock in gas propagates and its reflected shock wave focuses at the reverse side of the bubble, the temperature is enhanced so as to emit the luminosity.

It is well known that the oscillatory motion of a spherical bubble in a quiescent liquid creates the so-called sono-luminescence, in which at the moment of the bubble's minimum volume, the bubble emits light. However, unlike the sono-luminescence, the bubble emitted the luminosity, because of the wave interaction inside the bubble as seen in Fig. 13. The luminosity observed in Fig. 13 was hardly observable throughout holographic observation. This was based on the reasons that the holofilms did not have sensitivity to the luminous light and intense pulse laser beam always overexposed such faint luminosity.

Figure 13b shows the pressure history by embedding the FOPH pressure transducer into the wall. The ordinate designated pressure, in MPa and the abscissa designates time in  $\mu\text{s}$ . The first peak pressure at about 14  $\mu\text{s}$  corresponds to that occurred when the incident shock wave arrived at the wall, as seen in the fifth frame of Fig. 13a. The second peak pressure at about 20  $\mu\text{s}$  corresponds to which occurred when the secondary shock wave arrived at the wall, as seen in the eleventh frame. The pressure decrease at 22  $\mu\text{s}$  corresponds to the pressure decrease behind the reflected secondary shock wave from the wall as seen in the fourteenth frame.

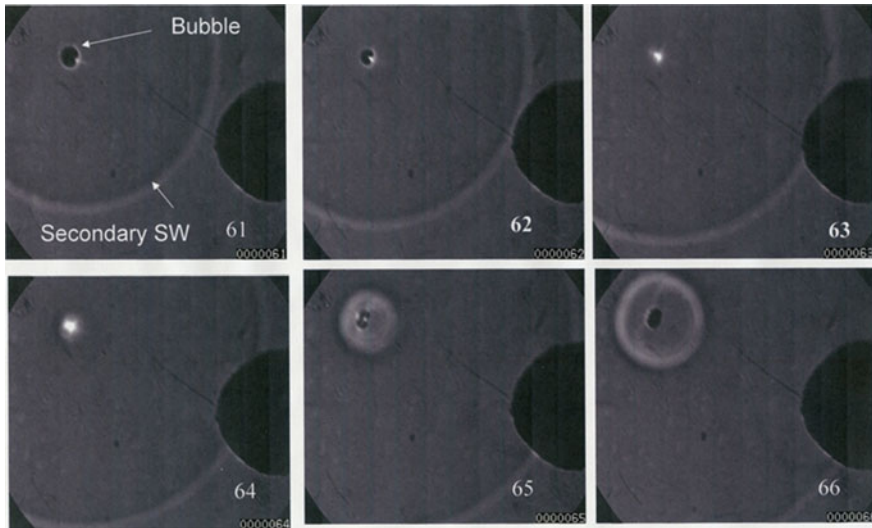


**Fig. 14** Emission of luminescence at shock/bubble interaction

As a next, the case of a spherical bubble was investigated. We placed a 1.5 mm diameter spherical air bubble at 20 mm stand-off distance and impacted it with a spherical shock of overpressure of about 40 MPa, which was generated by detonation of 10 mg  $\text{AgN}_3$  attached at the tip of an optical fiber. The visualization was carried out by using a direct shadowgraph and the images were recorded by a high-speed video camera, Shimadzu HVP-1, at the recording speed of 1,000,000 fps, the exposure time of 125 ns, and the total number of frame of 104.

Figure 14 show sequential images from the frame No. 61 to No. 66. In the frame 61, we can see the bubble on the left corner and the secondary shock wave as indicated by an arrows. The explosion product gas was shown as a dark irregular shadow at the right hand side.

In frames No. 62 and 63, the bubble contracted and the faint white spot in the frame No. 61 became brighter. In frame No. 64, the bright spot is most intense and large. The bubble is explosively enlarged, indicating the initiation of the secondary shock wave. From frame 64 to frame 65, although it is less accurate estimation, the secondary shock propagates at about  $M_s = 1.33$ , and from frame 65 to frame 66,  $M_s \geq 1.0$ . It should be noted that, as we already remarked in Fig. 9, the center of the secondary shock wave is located at the frontal stagnation point of the bubble. However, in the case of shock/non-spherical bubble interaction, the center of the secondary shock was shifted from the frontal stagnation point.

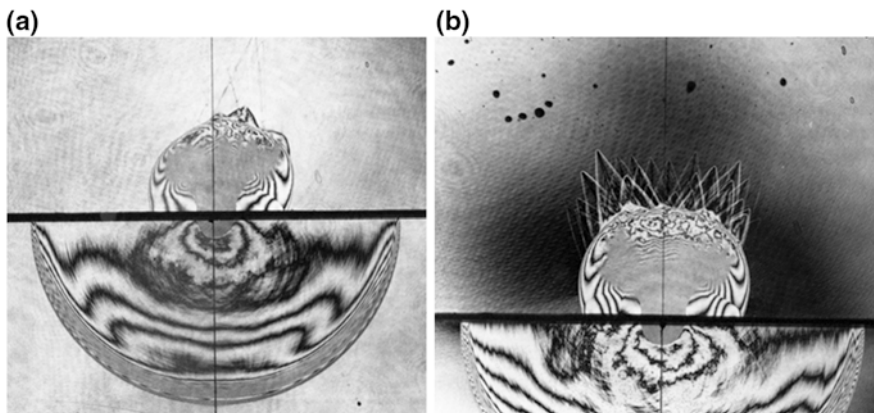
In Fig. 13 the bright spot appeared only temporarily in the 10th frame. This means that the emission took about a few  $\mu\text{s}$ . However, in Fig. 14, the emission continued for more than 4  $\mu\text{s}$ . The difference of the emission interval would be attributable to the wave propagation inside the bubble, in other words, the bubble shape.

## 8 Shock/Interface Interaction

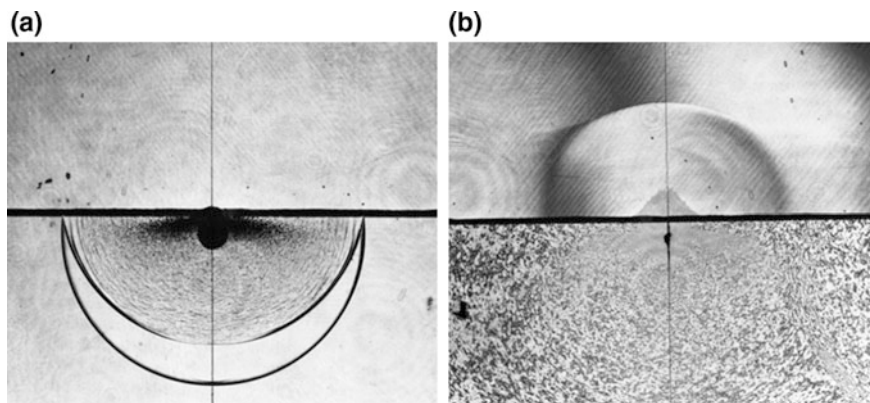
The interaction of shock waves generated by underwater explosions with gaseous interfaces or water/foreign liquid interfaces is one of the intriguing research topics, in particular, related to medical application of shock waves. Analytically, the point explosion at a gas/liquid interface is a singular problem. Waves in gas and liquid propagate independently. Hence, we performed series of experiments.

Figure 15a, b show double exposure holographic interferograms of a point explosion at an air/water interface. We submerged half of a 6.4 mg  $\text{PbN}_6$  pellet in water and ignited by irradiating a laser beam on it. In water, the spherically shaped explosion product gas drove a hemi-spherical shock wave, whereas in air the explosion product gas expanded not necessarily uniformly, but its top part ejected high speed debris and explosively vaporized water. Supersonic free flights of debris particles are clearly observable in Fig. 15b.

Hence, the top part of the explosion product gas formed a mushroom shaped shadow, which drove an irregularly shaped shock wave. The shock wave in air never looked neatly spherical. In short, the point explosion at the interface generates a hemi-spherical shock wave in water and although the shape is irregular, a little spherical shock wave is generated independently in air. As discussed, the energy transfer across a gas/liquid interface is governed by the acoustic impedances of each medium. The ratio of acoustic impedances is about 3450, so that energy in a gaseous phase is hardly transmitted into the liquid phase, and vice versa. The observation we saw in Fig. 15 would never agree with mathematical modeling. To improve the energy deposition, even if we may adopt a pulse laser beam deposition at the interface, the author would expect that the result would be much more complex. On the edge of the underwater shock front intersecting with the air, the fringe number sharply decreases, which implies that the underwater shock is locally attenuated.



**Fig. 15** Experimental verification of a singular point explosion at a gas/liquid interface, explosion of  $\text{PbN}_6$  6.4 mg at 1013 hPa and 284 K: **a** #83011807, 30  $\mu\text{s}$ ; **b** #83011808, 50  $\mu\text{s}$



**Fig. 16** Point explosion at 3 mm below air/water interface, explosion of 10 mg  $\text{PbN}_6$  at 1013 hPa and 288 K: **a** #83020202, delay time of 30  $\mu\text{s}$ , single exposure hologram; **b** #83020206, delay time of 70  $\mu\text{s}$

Figure 16a, b show the interaction of shock/air water interface visualized by double exposure holographic interferometry and a single exposure hologram. The shock waves were generated by explosion of 10 mg  $\text{PbN}_6$  submerged at 3 mm below the interface. The experimental condition was at atmospheric pressure and 288 K.

Although Fig. 16a was taken at first with the delay time of 30  $\mu\text{s}$ , we found from the distance of the shock traveled that this photo was taken at about 10  $\mu\text{s}$  after the ignition. When the shock wave impinged on the air/water interface, as the ratio of acoustic impedances between water and air is about is 3.400, the most of energy is reflected from the contact point and very small amount of energy in water is transmitted to the air.

The pressure should be high at the interface at 3 mm above the explosive. Then the interface at the contact point would move explosively upward. During 10  $\mu\text{s}$ , although not observable in this photo, the entire interface would move upward. Then the expansion wave was reflected. Along the center line, the interval between the reflected expansion wave and the shock wave is maintained to be 6 mm. Grey noises behind the reflected expansion wave indicate non-uniformly distributed bubble clouds. The flow around the explosion product gas is moving upward and the pressure at the center is gradually enhanced.

Due to the difference of acoustic impedance between water and air, only a fraction of energy in water is transmitted into the air. The energy is transmitted into the air, which created a visible change in fringes. The single exposure hologram missed the fringes. The shock wave created by the initial explosion attenuated with propagation and the reflected expansion wave followed just behind it.

In Fig. 16b, with the elapse of time, the interfacial deformation at the center is accelerated so that the shadow of the deformed interface shows a slightly jagged shape.

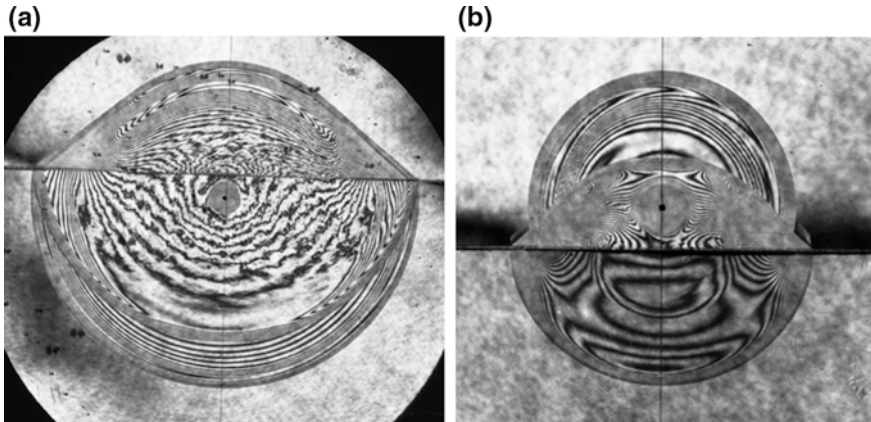


**Fig. 17** Shock interaction with water/silicon oil interface,  $\text{AgN}_3$  10 mg was detonated at 10 mm above the interface: **a** #92121502, water/10cSt silicon oil; and **b** #92123103, 10cSt silicon oil/water

We poured silicon oil on the surface of water and made a light/heavy liquid interface. Silicon oil 10cSt has sound speed of 960 m/s and is a safe liquid under normal conditions against explosion of  $\text{AgN}_3$  10 mg. We exploded the pellet at 10 mm above the interface. When detonating in water, we have a fast/slow interface as shown in Fig. 17a. When detonating it in silicon oil, we have a slow/fast interface as shown in Fig. 17b.

Sound speeds in water and silicon oil are 1500 and 980 m/s, respectively. Hence, the ratio of the acoustic impedance of water to that of silicon oil is about 1.8. In assuming a plane shock wave reflected from this interface, about 8% of energy in water is reflected and 92% of energy is transmitted into silicon oil. Hence, a spherical shock wave is generated at the central part in silicon oil. The shock wave in water propagates much faster than that in silicon oil and transmits an oblique shock wave into silicon oil. Hence, the shock wave in silicon oil looks like a combination of a spherical shock wave with an oblique shock wave as seen in Fig. 17a.

## 9 Reflection of Underwater Shock Wave

In gases, the transition of reflected shock waves is visualized, in shock tubes, shock wave reflection from metal wedges. In water, however, upon shock impingements on metal walls, longitudinal waves and shear waves are generated, which are precursory to the main shock waves and precise observations of their reflection is prevented. Avoiding such a complexity, Glass and Heuckroth [6] visualized the reflection of two underwater shock waves having identical strength. However,

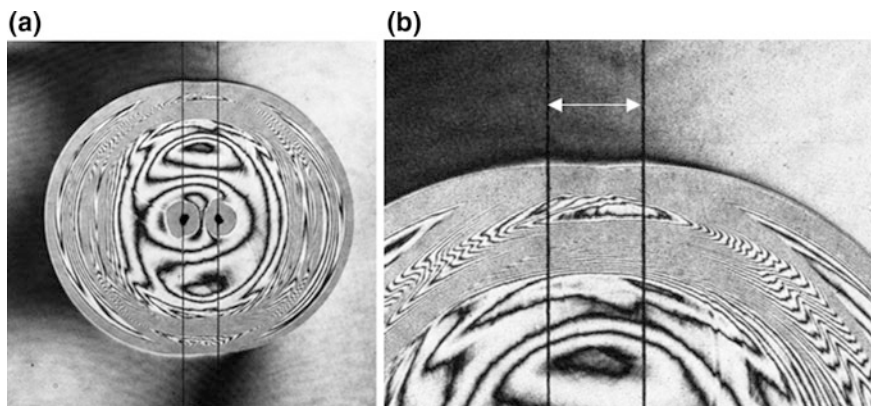


**Fig. 18** Reflection of underwater shock waves, simultaneous explosion of 6.2 mg and 6.3 mg  $\text{PbN}_6$  placed at 8 mm interval: **a** #83112805; and **b** Enlargement of (a)

the underwater shock waves thus created were not as strong as exhibiting Mach reflection patterns.

To achieve the generation of moderately strong underwater shock waves by explosion of  $\text{PbN}_6$  or  $\text{AgN}_3$ , we attached 6.2 mg and 6.3 mg  $\text{PbN}_6$  pellets each on a thin cotton thread, positioned them at an 8 mm interval and detonated them by the direct irradiation of a Q-switched ruby laser beam. Figure 18a shows a double exposure holographic interferogram. The delay time from the ignition to the visualization was 17  $\mu\text{s}$ . The elapsed time, if one estimated by assuming that the direct wave propagated at sonic speed, was 20  $\mu\text{s}$ . This implies that the direct wave propagated much faster than the sonic speed.

Figure 18b is enlarged image of Fig. 18a. The pattern of this intersection shows so-called von Neumann-Mach reflection (vNMR). This reflection pattern does not accompany any distinct triple points, which are a typical representation of gas-dynamic non-linearity. Therefore, vNMR appears usually when weak shock wave reflects from a shallow wedge. In other words, vNMR would appear when the flow behind the area in which the incident shock and the Mach stem merge is isentropic or nearly isentropic. Liquids are less compressible so that the particle velocity induced behind shock waves is low, even if the pressure is high. Hence, isentropic conditions are fulfilled so that the pattern of underwater shock wave reflections is mostly vNMR.

## 10 Underwater Shock Wave Focusing

Water is less compressible so that reflected underwater shock waves can be focused. A two-dimensional test section, 90 mm  $\times$  127.3 mm elliptical cavity (with ellipticity of  $2^{1/2}$ ) was machined on a 10 mm thick brass plate and sandwiched with

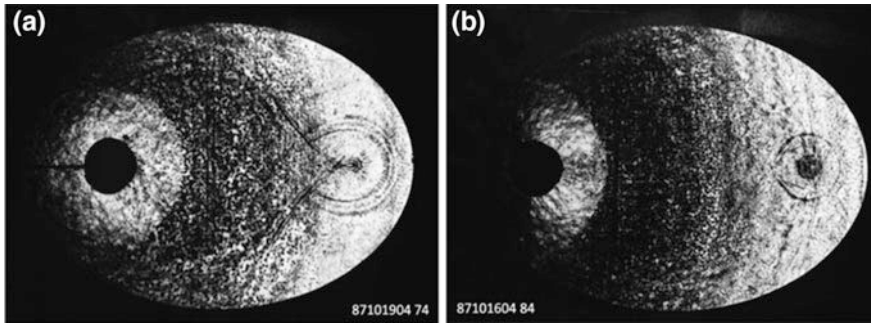


**Fig. 19** Two-dimensional shock wave focusing in a 90 mm  $\times$  127.3 mm elliptical cavity: **a** #84101904, 74  $\mu$ s; **b** #87101604, 84  $\mu$ s

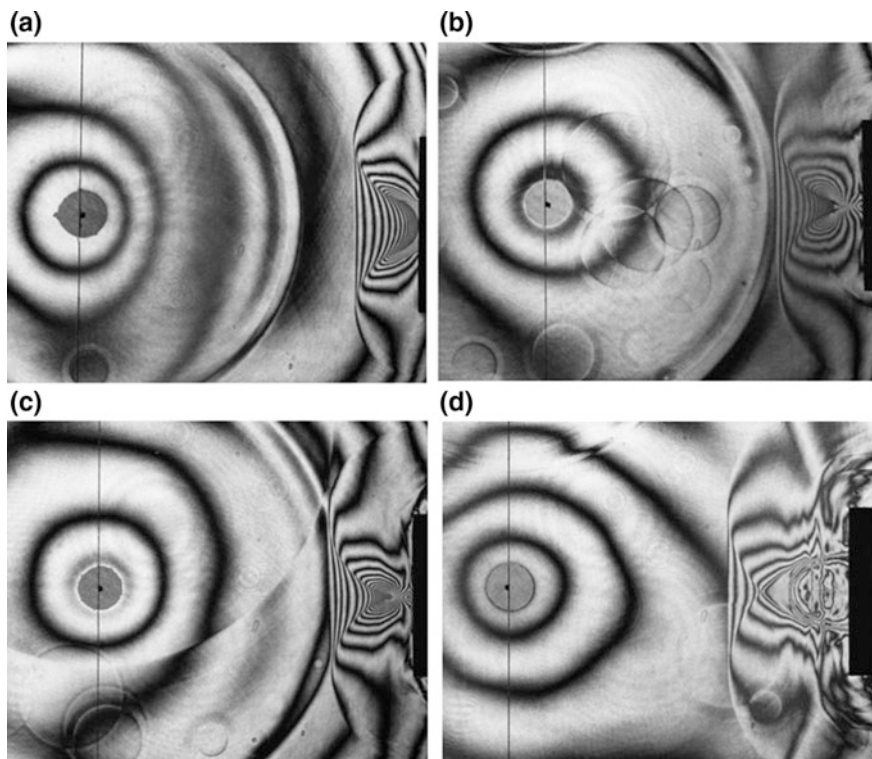
15 mm thick acrylic plates tightened with thick bolts. Filling water in the test section, we detonated a 4 mg  $\text{PbN}_6$  pellet at one of the focal points. At first a spherical shock wave was created, whose overpressures at 5 mm distance was well over 100 MPa. The high pressure quickly diminished. After multiple reflections between the two acrylic plates, the spherical shock wave eventually turned into a two-dimensional shock wave.

Figure 19 shows sequential direct shadowgraphs. Small dark spots distributed over the field of view show cavitation bubbles, which were instantaneously created as soon as the shock wave impacted the acrylic plates. Overpressures exceeding well 40 MPa made the acrylic plates move outward. Such a deformation instantaneously incepted cavitation bubbles. We never imagined that  $\text{PbN}_6$  4 mg pellets detonated at 5 mm distance deformed even 15 mm thick acrylic plates.

At first, we wanted to visualize test fields with a 5 mm distance from the explosive by using double exposure holographic interferometry. We then gave up to apply the idea and used a single exposure holographic method, that is, equivalence to direct shadowgraph. When a cylindrical shock was formed, it propagates and is reflected from the elliptic wall. Then, each segment of the reflected shock wave directs toward the second focal point. Numerical simulations or analytical comparisons with Fig. 19 would be rather straightforward. It would be worthwhile to study experimentally elongated elliptical cavities, in short with large ellipticity. However, it is an open question what will happen, if we try to focus reflected shock waves from a truncated ellipsoidal cavity.

We focused a reflected spherical shock wave generated at the first focal point of the ellipsoid which had the identical geometry as shown in Fig. 19 from a truncated ellipsoid of the same geometry. We wondered whether or not the reflected shock wave could focus at the second focal point. This was a part of a basic research of the shock wave application to medicine [8].

A 4 mg  $\text{PbN}_6$  pellet was detonated at the first focal point of the ellipsoid as shown in Fig. 20. The spherical shock wave is reflected from a 50 mm diameter truncated reflector, the bottom of which is located at about 109 mm from the focal



**Fig. 20** Shock wave focusing from a 50 mm diameter truncated reflector,  $\text{PbN}_6$  4 mg detonation at 1013 hPa and 285 K: **a** #83012111, delay time of 68  $\mu\text{s}$ ; **b** #83012012, delay time of 74  $\mu\text{s}$ ; **c** #83012103, delay time of 78  $\mu\text{s}$ ; **d** #83012128, delay time of 89  $\mu\text{s}$

point. In this arrangement, about 1.2% of the energy of the shock wave may be focused at the second focal point.

We took double exposure holographic interferograms sequentially at 2  $\mu\text{s}$  intervals. Selective images are shown in Fig. 20a–d. In Fig. 20a the spherical shock wave, which was generated at the first focal point, propagated, and hit the curved wall, was reflected. The reflected shock wave directed toward the second focal point. We can see the accumulation of fringes toward the second focal point. In Fig. 20b, the fringes are going to focus at the second focal point. The density locally concentrated so high that the object beam could not pass locally through this region. Hence the image of this region became dark and the fringes were no longer resolved.

Many faint double rings are observed. These are the remnants of reflected expansion waves and secondary shock waves released from bubbles on the test section windows. The bubbles were impinged by the shock wave created by the explosion of a 4 mg  $\text{PbN}_6$  pellet. The outer rings correspond to the reflected expansion waves and the inner rings correspond to the secondary shock waves,



which are now propagating at the sonic speed. The interval of the double rings corresponds to the delay time in which the secondary shock wave was created after the shock impingement on air bubbles on the window glass. At that time we did not clean the observation glass windows. Probably air bubbles of 1 mm diameter attached on the glass windows.

In Fig. 20b, the dense fringe concentration indicates the density increase at the second focal point, in other words, the pressure increase. The density is so high that the object beam was significantly refracted and did not pass straight. Hence, the fringes were not resolved in the focal region. The region looked grey.

Once again in Fig. 20, we are visualizing an axial symmetric flow field so that, unlike two-dimensional shock convergence, the fringe concentration indicates exponential increase in density and pressure toward the focal point. Counting fringes, we estimated the peak pressure to be 40 MPa at the focal point [8].

Within the limitation of the experimental accuracy, the point at which peak pressure appeared was deviated by 2 mm to the reflector [8]. Probably this would be attributable to the fact that the reflection of shock waves with finite strength from solid walls is slightly different from that of a sound wave and shock waves accompany flows which is more or less affected by the presence of the wall boundary layer

In Fig. 20c, the focal point looked grey and the peak pressure was achieved. Figure 20d shows a flow field after about 20  $\mu\text{s}$  from Fig. 20c.

We manufactured a 50 mm shallow dish having a 70 mm radius of curvature and 10.5 mm in depth and set it in a water chamber. We made a spherical shock wave reflect from the dish. We exploded a 10 mg  $\text{PbN}_6$  pellet at the 40 mm distance from the shallow dish and 25 mm away from its center line.

## 11 Remarks

In order to investigate cavitation phenomena, the bubble dynamic research and the underwater shock wave research complement each other, in which optical flow visualization plays an important role. Since 1980 we became interested in applications of underwater shock wave research to medicine, then realized and collected a little bit of knowledge. Today medical applications of shock wave research made progress. However, the author realized that to support the interdisciplinary work, one has to devote more enthusiasm to underwater shock wave research.

## References

1. N. Sanada, J. Ikeuchi, K. Takayama, O. Onodera, in *Generation and propagation of cavitation induced shock waves in a ultrasonic vibratory testing*, ed. by R.D. Archer, B. Milton (eds.), Proceedings of 14<sup>th</sup> International Symposium on Shock Tubes and Waves, (1983), pp. 405–412

2. K. Takayama, O. Onodera, H. Esashi, Motion of shock waves propagating over surfaces of liquids. *Mem. Inst. High Speed Mech. Tohoku Univ.* **48**, 419 (1982)
3. K. Takayama, Application of holographic interferometry to shock wave research. *Proc. SPIE* **298**, 174–180 (1983)
4. G. Ben-Dor, *Reflection of Shock Waves* (Springer, New York, 1980)
5. K. Takayama, H. Miyoshi, A. Abe, Shock wave reflection over gas/liquid interface, *Rep. Inst. High Speed Mech., Tohoku Univ.* **57**, 394 (1989)
6. I.I. Glass, L.E. Heuckroth, Low energy spherical underwater explosions. *Phys. Fluids* **11**, 2095–2107 (1968)
7. K. Takayama, Holographic interferometry study of shock wave propagation in two-phase media, in H. Groenig (ed.) *Proceedings of 16th international symposium on shock tube and waves* (1987), pp. 51–62
8. H. Esashi, *Study of shock wave propagation in liquids, Master Thesis* (Graduate School of Tohoku Univ, Faculty of Engineering, 1981)
9. N. Nagayasu, Study of shock waves generated by micro-explosions and their applications. *Doctoral Thesis, Graduate School of Engineering Tohoku University* (2001)
10. A. Shima, Studies on bubble dynamics. *SW J.* **7**, 33–42 (1997)
11. K. Ohtani, K. Takayama, Spherical shock wave interaction with a single gas bubble in liquids, *14th Cavitation Sym. Sendai* (2009)